The fast multi-frame X-ray diffraction detector at the Dynamic Compression Sector

N. W. Sinclair,[a]* S. J. Turneaure,[b] Y. Wang,[a] K. Zimmerman[b] and Y. M. Gupta[b]

[a]Dynamic Compression Sector (DCS), Institute for Shock Physics, Washington State University, Argonne, IL 60439, USA, and [b]Institute for Shock Physics and Department of Physics, Washington State University, Pullman, Washington, USA. *Correspondence e-mail: nicholas.sinclair@wsu.edu

A multi-frame, X-ray diffraction (XRD) detector system has been developed for use in time-resolved XRD measurements during single-event experiments at the Dynamic Compression Sector (DCS) at the Advanced Photon Source (APS). The system is capable of collecting four sequential XRD patterns separated by 153 ns, the period of the APS storage ring in the 24-bunch mode. This capability allows an examination of the temporal evolution of material dynamics in single-event experiments, such as plate impact experiments, explosive detonations, and split-Hopkinson pressure bar experiments. This system is available for all user experiments at the DCS. Here, the system description and measured performance parameters (detective quantum efficiency, spatial and temporal resolution, and dynamic range) are presented along with procedures for synchronization and image post-processing.

1. Introduction

Plate impact experiments are commonly used to achieve well-characterized, controlled compression states on short time-scales (ns to µs) in condensed matter. Although such experiments have a long history of providing valuable thermo-dynamic data at extreme conditions, *in situ* measurements of structural changes at the atomistic level and direct determination of lattice parameters in such experiments constitute important scientific challenges. The need for such measurements was the motivation for the development of the Dynamic Compression Sector (DCS) — Sector 35 of the Advanced Photon Source (APS). The DCS is a user facility dedicated to time-resolved X-ray measurements in materials subjected to dynamic compression using a variety of platforms, including single-stage and two-stage gas-guns.

To examine the temporal evolution of structural changes in shockwave, or dynamic compression, experiments — which are inherently destructive — requires a series of X-ray diffraction (XRD) measurements. These measurements must be collected during a single experiment or there must be an assumption that subsequent experiments will be sufficiently similar to compare across experiments, a degree of similarity which is difficult to achieve, costly to demonstrate, and always subject to doubt. The X-ray beam from the APS storage ring is particularly well suited for this requirement, as it provides a high-frequency, repetitive pattern of X-ray 'bunches' to probe the sample. A custom multi-frame detection system has been developed to meet these requirements. While user experiments employing this detector system have already led to many scientific publications, this article describes the detector system's operation and capabilities in detail, along with complications arising from its particular design, with the aim
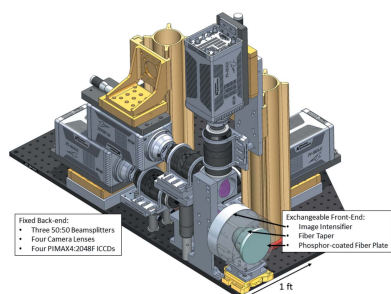

Fixed Back-end:
• Three 50:50 Beamsplitters
• Four Camera Lenses
• Four PIMAX4:2048F ICCDs

Exchangeable Front-End:
Image Intensifier
Fiber Taper
Phosphor-coated Fiber Plate

1 ft

Table 1
Detector parameters for each fiber taper size.

Fiber taper	Active area diameter	Relative taper optical loss	PSF (FWHM)	Spatial calibration	DQE
75:40 mm	76.0 mm	1	220 μm	1 mm / 23 pixels	Measured†: 0.4 to 0.6 Expected‡: 0.3
120:40 mm	121.3 mm	2.7× Lower signal	350 μm	2 mm / 29 pixels	Expected‡: 0.14
150:40 mm	152.0 mm	8× Lower signal	440 μm	2 mm / 23 pixels	Expected‡: 0.05

† At 23 keV, with all gain settings at maximum. This will vary with configuration (intensifier gain and phosphor).   ‡ Estimated from measured and estimated component parameters.

of clarifying its operation for beamline users and pointing out potential areas of improvement for future high-speed, indirect detection systems.

For the desired measurements, the detector must have high sensitivity over a broad range of X-ray energies (7 keV to 35 keV) and be able to maintain linearity for a large signal flux. For XRD experiments at the DCS, the undulator is typically configured to deliver a high X-ray flux, 7×10^{15} photons s^{-1}, at 23 keV. Since no monochromator is used to filter this beam, the high peak flux during a bunch precludes the use of photon-counting area detectors. Most fast, direct-detection pixel-array detectors (PADs) employ Si as the X-ray absorption medium, limiting the X-ray energies to well below 20 keV for high quantum efficiency (QE). For example, the AGIPD (Allahgholi *et al.*, 2019), LPD (Hart *et al.*, 2012) and the Keck PAD (Philipp *et al.*, 2016) all use silicon with a thickness of 0.5 mm, while the attenuation length of Si at 23 keV is 1.6 mm. Advances are being made to develop PADs with higher density active media (Becker *et al.*, 2016), and these approaches may lead to a more optimized detector in the future. However, the current DCS X-ray diffraction detectors employ indirect detection using an X-ray phosphor, since this can provide high absorption efficiency in the range of 20 keV with coating thicknesses on the order of 100 μm.

For many impact experiments, the interesting structural changes may be contained in only one or two diffraction patterns of the four collected, since only one of the images may be required to compare the ambient and peak stress states. However, multi-frame capability remains vital for two primary reasons. First, it provides a margin for error in timing the detectors with respect to impact, allowing for small variations in the projectile velocity. Second, the other frames allow verification of the context of that single frame, verifying that the preceding and subsequent frames show the expected dynamics, *e.g.* ambient conditions, stress release, *etc*. As impact experiments are both complex and destructive, not allowing precise reconstruction of the experimental conditions, observing the XRD pattern evolve is an invaluable capability to ensure the validity of the experiment.

Previously, a single-frame version of this detector system proved effective for capturing XRD snapshots from a single X-ray pulse during impact experiments (Gupta *et al.*, 2012). That system consisted of an X-ray phosphor, a fiber optic taper, an image intensifier, and a CCD camera. This geometry was similar to that of existing commercial indirect X-ray detectors [*e.g.* the Rayonix SX165 (Rayonix LLC, 2021)],

except exchanging the high-brightness scintillator (terbium-doped gadolinium oxysulfide on the SX165) for a faster scintillator, Y_2SiO_5 doped with cerium (P47), and adding an image intensifier for gain and temporal resolution. Similarly, Luo *et al.* (2012) used a fiber taper and an intensified CCD camera (ICCD) to capture a single-bunch XRD pattern during a shock experiment. Luo *et al.* (2012) also demonstrated a phase-contrast imaging detection system capable of capturing two sequential frames separated by 153 ns, the time between X-ray bunches in the '24-bunch mode' of the APS storage ring, by using two ICCDs and optical beam-splitting. That beam-splitting approach was facilitated by the much higher signal level of direct beam imaging over XRD detection. Creating a four-frame XRD detector with large active area requires a combination of these approaches, with the addition of both beam-splitting optics and an additional amplification stage, in the form of a second image intensifier. The DCS diffraction detector employs an image intensifier to amplify the signal before splitting to four time-resolved ICCDs to collect four sequential XRD images. This cascading amplification adds complexity to the detector trigger timing, and it also causes some contamination of the images from preceding X-ray bunches. Both of these issues are examined in detail in subsequent sections to clarify the requirements for optimal operation and data analysis.

To date, this system has been used successfully in impact experiments (Turneaure *et al.*, 2016, 2017; Newman *et al.*, 2018; Tracy *et al.*, 2018; Renganathan *et al.*, 2019), time-resolved small-angle X-ray scattering (SAXS) experiments on detonating explosives (Bagge-Hansen *et al.*, 2015), and Kolsky bar experiments (Lambert *et al.*, 2020). In these experiments, the detector system has demonstrated sufficient sensitivity to measure XRD powder rings and SAXS patterns from a single X-ray pulse. The system is quite flexible; it can be configured with an active region diameter of 75 mm, 120 mm, or 150 mm and with interchangeable X-ray phosphor plates to optimize for different X-ray photon energies. Table 1 displays important parameters of the detector system for each of the available active region diameters. These parameters are explained in detail in subsequent sections.

The system components and overall operation of the detector are described in the next section. Subsequent sections describe the temporal and spatial resolution, a correction method for removing the contamination from preceding X-ray exposures, methods for distortion correction and frame-alignment, and a measurement of the detector's detective

quantum efficiency (DQE). Example data are presented in Section 8 to illustrate XRD data from a typical impact experiment and the application of the post-processing techniques.

2. System description

The four-frame detector system includes a modular front-end, that can be easily reconfigured, and a fixed back-end. The front-end consists of an X-ray phosphor-coated fiber optic plate, a fiber optic taper, and a microchannel plate (MCP) image intensifier. The back-end consists of beam-splitters, four camera lenses, and four ICCD cameras. A model of the system is displayed in Fig. 1. The overall sequence of photon propagation is as follows: (1) X-ray photons are converted to visible light using a fast X-ray phosphor on a fiber optic plate, (2) the image is demagnified with a fiber taper, (3) a fiber-coupled image intensifier provides gain and emits the image from its own fast phosphor, (4) the light is split into four paths using 50:50 beam-splitters, (5) the split light is imaged onto four ICCD photocathodes with individual camera lenses, and (6) each ICCD is gated to capture an exposure from a single X-ray pulse.

The X-rays scattered from the sample are converted to visible light through the use of a fast X-ray phosphor. Lutetium oxyorthosilicate doped with cerium (Lu_2SiO_5:Ce, LSO:Ce) is used, due to its brightness and short decay lifetime. The powdered LSO:Ce coats the surface of a large fiber optic plate (Incom, Inc.), with a diameter of 75 mm, 120 mm, or 150 mm. To demagnify the output of this large plate for capture by a camera, the fiber optic plate is coupled to a fiber optic taper (Incom, Inc.), decreasing the image diameter to 40 mm (a demagnification factor of 1.875 for the 75 mm taper).
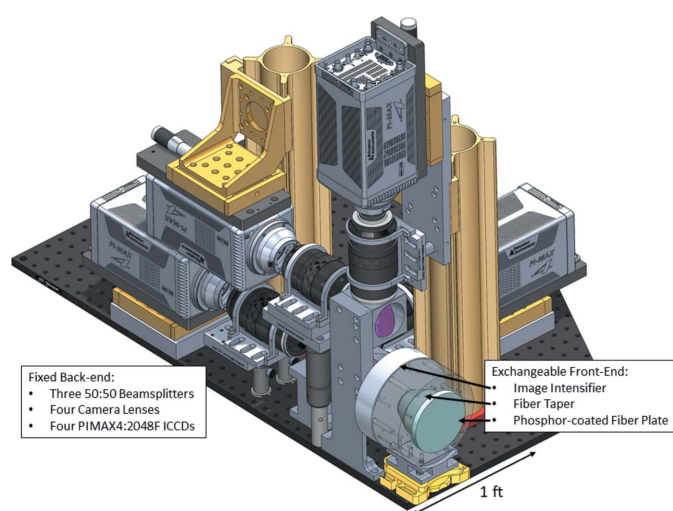

Figure 1
Model of the four-frame detector system. X-rays enter the system at the bottom right of the image, where the front of the fiber optic plate is coated with LSO:Ce X-ray phosphor. This fiber plate is coupled to a fiber taper and then to an image intensifier. The image intensifier's phosphor screen anode emits light, which passes through three beam-splitters and is focused on four ICCD cameras. The kinematic mounting of the front-end (phosphor, taper, and intensifier) allows the system to be easily modified.

The light exiting this taper is directly coupled to the MCP image intensifier (Photek MCP140), which has a fiber optic input window to the S20 photocathode. Index matching fluid with a refractive index of 1.6 is used between all fiber optic surface connections to facilitate light transmission. This image intensifier exists only to provide gain, not to achieve time resolution with its gating capability. According to the manufacturer's test report, the achievable gain level for this intensifier, the ratio of radiant exitance to irradiance, is up to 4000. The photocathode is typically gated on for 1–2 µs before images are taken, long enough to allow the gating voltage across the photocathode-MCP gap to equilibrate across the active area but short enough to minimize saturation of the MCP due to the large electron flux. The intensifier anode is a P47 phosphor screen, emitting visible light to the downstream ICCD detectors.

The X-ray phosphor, fiber taper, and image intensifier comprise a modular front-end that can be configured in multiple ways to accommodate a variety of needs. The undulators at the DCS provide a continuously tunable range of X-ray energies from 7 keV upward, reaching much higher X-ray energies with the higher undulator harmonics. To optimally collect this wide range of X-ray energies, different phosphor thicknesses are desirable. In addition, the size of the detector's active area is a compromise between angular resolution, angular range, and signal intensity, per user priorities. Consequently, this system has been designed to allow the front-end to be easily removed and reinstalled via a kinematic mount, as shown in the bottom portion of Fig. 1. Once removed, the front-end may be easily disassembled, and the fiber optic taper may be swapped for one with a different demagnification. At the same time, the phosphor-coated plate may be swapped for one with a different coating thickness and a diameter suited for the chosen demagnification.

To avoid delivering unnecessarily large X-ray doses to the fiber plate, the X-ray beam is dynamically shuttered. For impact experiments, the shutter system at the DCS is configured to be open for tens of milliseconds, long enough to account for the uncertainty in impact timing. During ambient images, the exposure times are reduced to about 20 µs. In this configuration, we have not observed any localized degradation of the detector performance that we might expect from overexposure to an XRD pattern. However, exposure of the fiber plate to the direct beam for tens of milliseconds (*e.g.* if the X-ray beamstop is not fully blocking the beam) will discolor the plate in the exposed area through the generation of color centers in the glass. While this does not happen during normal operation, the ability to easily exchange the phosphor-coated plate allows this to be quickly remedied.

Light emitted from the image intensifier on this modular front-end is transmitted to the fixed back-end. The light is split, using three 50:50 plate beam-splitters to four F-mount camera lenses (Zeiss Makro-Planar T* 100 mm $f/2$ ZF.2), each imaging the intensifier emission onto the photocathode of one of the four ICCD cameras (PIMAX4:2048f). The ICCDs have a 25 mm circular image intensifier, coupled to a CCD with 2048 × 2048, 13.5 µm pixels. The image intensifier of each

Fixed Back-end:
- Three 50:50 Beamsplitters
- Four Camera Lenses
- Four PIMAX4:2048F ICCDs

Exchangeable Front-End:
- Image Intensifier
- Fiber Taper
- Phosphor-coated Fiber Plate

1 ft

camera is gated to collect predominantly the emission from a single X-ray pulse. Finally, the image intensifier inside each ICCD camera has a P43 phosphor on its anode that converts the electrical signal back to light for capture by the CCD. The total demagnification from the phosphor plate to the CCD, for the 75 mm taper, is typically a factor of 3.2.

The two phosphors prior to the ICCD gating, LSO:Ce and P47, both have short decay lifetimes, and they were chosen to minimize the temporal overlap of the luminescence from sequential X-ray pulses. The remaining phosphor, the P43 on the output of the ICCD's intensifier, does not contribute to the bunch discrimination because it is after the ICCD photocathode gating. To clarify the role of the phosphor decays, Fig. 2 shows the temporal structure of the light intensity at each stage in the collection process: (a) as the X-rays arrive at the phosphor, (b) as the visible light is emitted from the X-ray phosphor (LSO:Ce), and (c) as the visible light is emitted from the image intensifier's P47 anode screen. Fig. 2(a) shows the pattern of X-ray pulses delivered to the detector in the 24-bunch mode, with each exposure occurring 153.4 ns apart. Fig. 2(b) shows the emission from the LSO:Ce due to this excitation, modeled by a single-exponential decay with 43 ns e^{-1} lifetime, which matches measurements of its decay for the first 150 ns. Fig. 2(c) shows the modeled time structure of the P47 phosphor output, after illumination by the LSO:Ce phosphor pattern displayed in Fig. 2(b). Fig. 2(c) also shows the four ICCD gates used to collect the phosphor emission. Despite the relatively fast decay of each of the

phosphors, it is clear from Fig. 2(c) that each camera gate will collect some light from previous X-ray exposures. This is discussed in detail in the following section, where it is shown that in a typical configuration the CCD would collect 80% of the emission from the desired pulse and 14% of the previous pulse. Since the phosphor decays are so extended, the ICCD gates must be both long and precisely timed to optimally collect the emission from a single X-ray pulse. The next section discusses both the timing of these ICCD gates as well as the model employed to describe the P47 emission.

3. Temporal resolution and X-ray synchronization

The degree to which this camera system may distinguish an image of one X-ray bunch from surrounding bunches is governed by the pattern of X-ray bunches, the response of the two phosphors, and the timing of the photocathode gating in the ICCD. To quantify the expected performance, it is worth examining each of these aspects in detail.

The APS storage ring typically provides three common storage ring modes, the 24-bunch mode with evenly spaced bunches at 153 ns interval, the 'Hybrid' mode, having one high-current electron bunch on one side of the storage ring and eight groups of closely spaced septuplet bunches on the other, and the '324-bunch' mode, with equally spaced X-ray pulses separated by only 11 ns. The spacing of the 324-bunch mode is too short with the current phosphors to discriminate sequential bunches, and the Hybrid mode may be used by concentrating on the single bright pulses with a frame rate of 271.6 kHz. The system was designed to operate during the 24-bunch mode with bunches evenly spaced, 153.4 ns apart, with a single burst exposure of four frames. Since the readout time is on the order of seconds, this detector is not suitable for repeated bursts in a single experiment.

The detector acquisition must be synchronized to the impact event as well as the precise arrival of X-ray bunches at the detector. The dynamic experiment provides a trigger to determine when the detectors should begin taking images (e.g. from a projectile breaking an optical beam near the sample or striking a piezoelectric pin); in most cases, this signal cannot be synchronized to the storage ring. For example, the impact event during a plate impact experiment cannot be synchronized precisely to the arrival of an X-ray bunch because the jitter in the gun's fire-to-impact time is on the order of milliseconds. Therefore, the synchronization with the experiment and X-ray arrival is accomplished in two steps. After the trigger from the experiment, each camera's photocathode gate must be carefully timed off of a synchronization signal at the bunch frequency (6.52 MHz in 24-bunch mode) in order to discriminate one X-ray pulse from the next. The storage ring provides the 'bunch clock' signal for this purpose. After the experimental trigger, the detectors are triggered on the next bunch clock signal from the ring and thus synchronized to both the ring frequency and the dynamic experiment. This synchronization process leads to an uncertainty in predicting the exposure time with respect to the experimentally generated trigger of one inter-bunch spacing (153.4 ns in the 24-
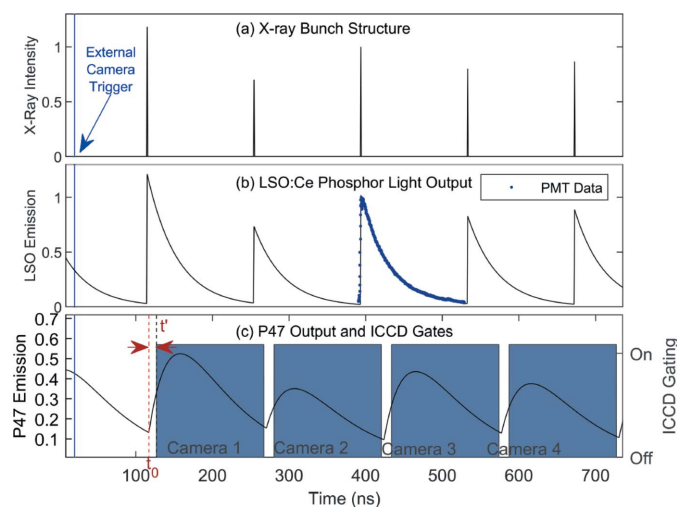

Figure 2
Timeline of X-ray excitation and visible light emission during acquisition. The three aligned axes in this figure show the temporal structure of the light intensity at each stage in the conversion process: (a) the X-ray bunch structure in 24-bunch mode, with a 90 ps X-ray bunch arriving at the detector every 153.4 ns; (b) the modeled emission from the LSO:Ce X-ray phosphor under illumination from this X-ray bunch pattern; and (c) the modeled response of the P47 phosphor to the LSO:Ce emission as well as the timing of the ICCD gates to collect the P47 emission. The ICCD gating windows are shown by the shaded blue regions. The ICCD gates are delayed from the experimental trigger to capture the data of interest and to optimize the collection of emission from each X-ray bunch.

bunch mode). After the experiment, however, the precise time that the X-rays probe the sample relative to the dynamic event may be determined by comparing the timing of the impact event to the synchronized detector trigger, with an uncertainty on the order of a nanosecond.

The bunch clock signal from the storage ring does not coincide with the arrival time of light at the ICCD photocathode. It is simply a signal with the proper frequency and an arbitrary phase. Hence, an additional delay must be added after the bunch clock trigger to properly align the camera gates to the phosphor emission from each X-ray pulse. The relative delay between the start of an ICCD gate and light arrival from an X-ray bunch at the ICCD photocathode determines the degree of the bunch isolation achieved. More precisely, this delay determines the efficiency of collecting light from the X-ray bunch of interest and the brightness of the 'after-image' seen from the previous bunch due to the extended phosphor decays. To properly set this gate delay, one must first determine the time of arrival of the first light from an X-ray bunch at the photocathode. Then, one can choose an optimal delay after this arrival time to maximize the collection efficiency and minimize the after-image.

To determine the ICCD gate delay corresponding to the time of arrival, t_0, of the first light from an X-ray bunch, the ICCD signal may be measured as a function of gate delay. This arrival time can then be extracted as a fitted parameter, using a modeled response function for the combination of the LSO:Ce and P47 phosphors in series. The temporal pattern of the P47 emission will be a convolution of the LSO:Ce decay and the response of the P47 phosphor to a delta-function input. From a single, infinitesimally short X-ray pulse arriving at two phosphors in series, each with pure, single-exponential decays, τ_1 and τ_2, the emission rate from the second phosphor would have a simple functional form, given by

$$R_{\text{single}}(t) = \frac{A}{\tau_1 - \tau_2} \left[\exp\left(-\frac{t - t_0}{\tau_1}\right) - \exp\left(-\frac{t - t_0}{\tau_2}\right) \right]$$
$$\times H(t - t_0), \tag{1}$$

where $H(t)$ is the Heaviside step function and A is a fitting constant. Most commonly, the data used for this fitting will be collected in the 24-bunch mode, where it cannot be treated as an isolated pulse. In this case, for an infinite series of pulses, each separated by time Δ, the emission rate can be treated as periodic, as the sum of equation (1) over an infinite sequence of bunches,

$$R_{\text{periodic}}(T) = \left(\frac{A}{\tau_1 - \tau_2}\right) \left[\frac{\exp(-T/\tau_1)}{1 - \exp(-\Delta/\tau_1)} - \frac{\exp(-T/\tau_2)}{1 - \exp(-\Delta/\tau_2)} \right],$$
$$T = (t - t_0) \bmod \Delta. \tag{2}$$

This function has the shape seen in Fig. 2(c), showing the temporal profile of the P47 emission.

For simplicity of notation, we ignore the short propagation delay between the second phosphor and the ICCD photocathode and treat t_0 as the time of first light arrival at the ICCD photocathode. In this case, the signal level seen in an ICCD exposure is given by equation (2), integrated over the ICCD gate duration. This will serve as the fitting function for the ICCD data used to determine t_0. Fig. 3 shows an example of the data collected for this timing measurement in the 24-bunch mode, along with the fit to determine t_0. The ICCD gate duration is held fixed at 7 ns (though any width that is short compared with the signal rise time will suffice), while the gate delay is swept over one bunch period. The background counts have been subtracted, so the remaining counts seen before the next bunch arrives are the residual excitation from the previous pulses. The two phosphor lifetimes, τ_1 and τ_2, are fixed at 26.2 ns and 70.4 ns, and t_0 is fitted to the data. The two phosphor lifetimes are determined from a fit to a separate data set, collected during the Hybrid mode, with a separation between pulses of 1.6 µs and, consequently, negligible overlap of the phosphor decays. These data and fit are included as an inset to Fig. 3, showing good agreement to delays beyond 400 ns from pulse arrival.

It should be noted that the lifetime parameters determined in the fitted model should not be interpreted as the individual decay lifetimes of LSO:Ce and P47, despite this being their origin in equation (2). Each of these phosphors also has a longer decay component that is apparent at late times. Conveniently, these complicated decays can be captured approximately by allowing the model parameters to deviate from the actual e^{-1} lifetimes of each phosphor. The accuracy of the fitting in the inset of Fig. 3 demonstrates that this approximation is acceptable.

Once t_0 is determined from the fit, the ICCD gate timing relative to t_0 should be set to maximize collection of the emission from the desired bunch and minimize the collection
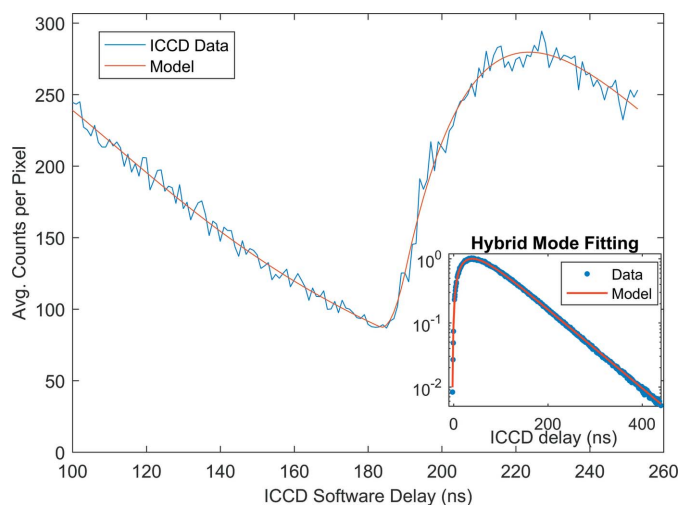

Figure 3
Determination of the light arrival time at the ICCD. The ICCD signal is measured with varying gate delay after bunch clock synchronization during the 24-bunch mode, in which X-ray pulses arrive every 153.4 ns. The gate width is fixed at 7 ns, shorter than a normal experimental gate, to increase contrast in the signal as a function of delay. The light arrival time is fitted using the model of equation (2), of two sequential phosphors with single exponential decays and lifetimes of 26.2 ns and 70.4 ns. These lifetime parameters were determined from a fit of equation (1) to similar data taken in the Hybrid mode (inset), where X-ray pulses are separated by 1.6 µs.

of light from previous bunches. To examine the optimal photocathode timing and degree of contamination from previous bunches, we will examine the collection efficiency versus gate delay. We define the gate collection efficiency from each pulse, $\eta(t', \delta t)$, as the fraction of the total light incident on the ICCD photocathode from one X-ray pulse collected during an ICCD gate, where t' is the delay of the start of the ICCD gate from t_0 and δt is the gate duration. So, $\eta(t', \delta t)$ is a measure of the efficiency of a set of gate timing parameters, and it is given by

$$\eta(t', \delta t) = \int_{t'}^{t'+\delta t} R_{\text{single}}(t)\, \mathrm{d}t \qquad (3)$$

$$= \begin{cases} \sum_{k=1,2} \frac{(-1)^k \tau_k}{\tau_2 - \tau_1} \left\{ \exp\left(-\frac{t'}{\tau_k}\right) - \exp\left[-\frac{(t'+\delta t)}{\tau_k}\right] \right\}, & \text{if } t' > 0, \\ \sum_{k=1,2} \frac{(-1)^k \tau_k}{\tau_2 - \tau_1} \left\{ 1 - \exp\left[-\frac{(t'+\delta t)}{\tau_k}\right] \right\}, & \text{if } -\delta t < t' < 0, \\ 0, & \text{if } t' < -\delta t. \end{cases}$$

To quantify the degree of after-image observed, this equation may also be used to quantify the amount of the light collected from the residual phosphor decays of a preceding X-ray pulse by shifting t' to represent the gate delay from the t_0 of that pulse. For example, in the 24-bunch mode, an image collected with a 140 ns gate beginning at $t' = 6$ ns collects $\eta(6\text{ ns}, 140\text{ns})$ of the 'target' pulse that began 6 ns earlier at t_0, $\eta(6\text{ ns} + 153.4\text{ ns}, 140\text{ ns})$ of the preceding pulse that began at $(t_0 - 153.4\text{ ns})$, $\eta(6\text{ ns} + 2 \times 153.4\text{ ns}, 140\text{ ns})$ of the X-ray pulse prior to that, *etc*. In addition, if the gate is poorly timed such that the gate overlaps the next pulse, equation (3) can be used to predict the collected fraction from the subsequent pulse by subtracting 153.4 ns from t'.

To illustrate the dependence of the collection efficiency and quantity of after-image from previous pulses on the gate delay, Fig. 4(a) shows $\eta(t', 140\text{ ns})$, $\eta(t' + 153.4\text{ ns}, 140\text{ ns})$, and $\eta(t' - 153.4\text{ ns}, 140\text{ ns})$, the collected fraction of the 'Target' pulse, the 'Previous' pulse, and the 'Next' pulse, respectively, as a function of t'. For a 140 ns gate, the maximum efficiency for collecting the target pulse is just under 80% with a delay of 6 ns; at this delay, the ICCD would still capture 14% of the light emitted from the previous X-ray pulse.

The important figure for quantifying the after-image is the relative collection efficiencies of the previous pulses compared with that of the target pulse,

$$F_m(t') = \frac{\eta(t' + m\Delta, \delta t)}{\eta(t', \delta t)}, \qquad (4)$$

where $F_m(t')$ represents the relative collection efficiency of the mth prior pulse. Fig. 4(b) displays $F_1(t')$, the relative collection efficiency of the previous pulse, where it is clear that the relative proportion of the after-image decreases monotonically with increasing gate delay from t_0. When the maximum collection efficiency occurs for the target pulse, at $t' = 6$ ns, the collection efficiency of the previous pulse is 17.8% of that of the target pulse. In order to minimize the after-image, one might be inclined to set a longer gate delay.
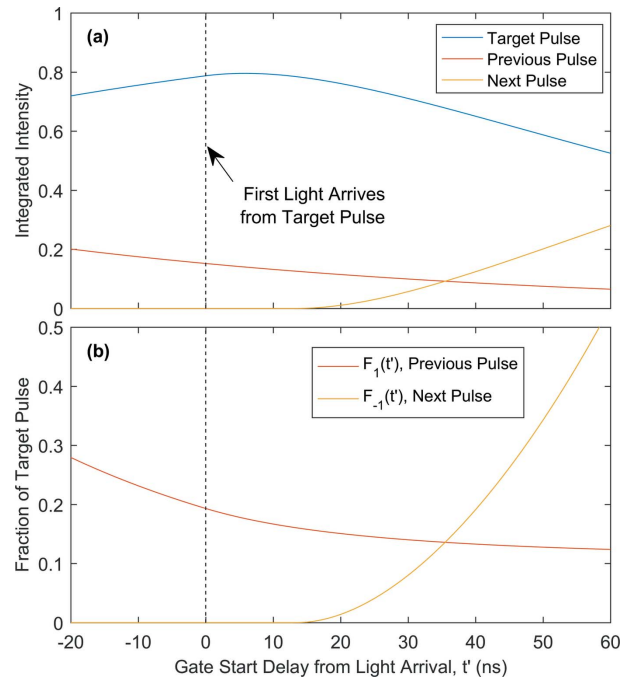

Figure 4
Optimization of ICCD gate timing parameters. (*a*) The ICCD collection efficiency, $\eta(t', 140\text{ ns})$, of a 140 ns duration gate with varying gate delay from first light arrival at the ICCD photocathode, t', as predicted by equation (3). (*b*) The relative collection efficiencies, $F_1(t')$ and $F_{-1}(t')$, of the previous X-ray pulse and next X-ray pulse, respectively, as a function of gate delay. $F_1(t')$ represents the relative weight of the after-image due to the previous pulse in comparison to the weight of the pulse of interest.

However, the improvements in the after-image are slight compared with the loss in signal. Since some degree of after-image is unavoidable with this detection scheme, a procedure for subtraction of the after-images to obtain uncontaminated single-pulse images is discussed in Section 4.

The temporal resolution of a measurement on this detector is determined by how well the images from separate X-ray pulses can be discriminated. This discrimination can be achieved if either the after-image subtraction described in Section 4 is performed or if the detector patterns from subsequent bunches are sufficiently distinct that the features of interest do not overlap. For XRD experiments at the DCS, the latter condition is often true and subtraction is not necessarily required for determination of structural parameters. For example, when observing a structural phase transition, the new diffraction peaks may be very distinct from those of the previous phase. In the work of Turneaure *et al.* (2016) regarding the cubic diamond to simple hexagonal transition in silicon, only one of the visible diffraction peaks from each phase overlapped significantly, so the change in phase was easily identifiable. In such measurements, where the images from separate exposures are discernible, the effective X-ray exposure time for each measurement is the X-ray pulse duration, which is about 90 ps FWHM (Sajaev, 2010), varying slightly with the electron bunch current. However, in cases where measurements from sequential bunches cannot be isolated, when the after-image correction cannot be performed

and when the patterns overlap significantly from pulse to pulse, this 90 ps exposure time is not an accurate description. In such cases, a measurement in the 24-bunch mode represents a sequence of 90 ps exposures separated by 153.4 ns, with collection efficiencies given by $\eta(t' + m\Delta, \delta t)$.

If the detector is used during the Hybrid mode, the data will show no significant after-image contamination, due to the large separation between X-ray exposures. The detector may also be used during the 324-bunch mode by integrating over several pulses, but with poorer time resolution than in the 24-bunch mode. Using this detector, both of these modes are more useful for longer time-scale experiments, where the lower repetition rate of Hybrid mode is acceptable, or where the integration over many bunches in 324-bunch mode would not cause significant blurring of the images.

4. After-image subtraction

Since the detector collects sequential frames, it is possible to subtract the after-images using the knowledge of the previous frames. The relative brightness, $F_m(t')$, of the mth previous frame relative to that of the desired frame can be calculated from equations (3) and (4). This discussion will be limited to data collected in the 24-bunch mode of the storage ring, with a 153.4 ns separation between bunches. Data from individual pulses in the Hybrid mode do not need correction due to the large separation between pulses. In the 24-bunch mode, for the highest efficiency gate delay with a 140 ns gate, $t' = 6$ ns: $F_1 = 0.178$, $F_2 = 0.020$, and $F_3 = 0.0023$, so it is clearly desirable to subtract the previous frame and potentially useful to subtract the frame before that.

Ignoring for the moment that there are a very limited number of frames to potentially subtract, one can write down a general expression for the real intensity producing the image of the Nth X-ray pulse, $\mathcal{I}_{\text{real}}^N$, uncontaminated by after-images, determined from a series of sequentially collected images, $\mathcal{I}_{\text{coll}}^N$, each contaminated with portions of every preceding X-ray pulse,

$$\mathcal{I}_{\text{real}}^N = \frac{\mathcal{I}_{\text{coll}}^N}{\eta(t', \delta t)\chi^N} - \sum_{i=1}^{N-1} F_i \frac{\mathcal{I}_{\text{coll}}^{N-i}}{\eta(t', \delta t)\chi^{N-i}}$$
$$\sum_{i=1}^{N-1} \sum_{j=1}^{N-1-i} F_i F_j \frac{\mathcal{I}_{\text{coll}}^{N-i-j}}{\eta(t', \delta t)\chi^{N-i-j}} - \dots \quad (5)$$

where χ^N is the total conversion gain (photons to counts) of the camera used to collect an image $\mathcal{I}_{\text{coll}}^N$ and $\eta(t', \delta t)$ is given by equation (3). We have assumed that the gate delay and duration are short enough to not overlap the next frame, i.e. $t' + \delta t$ is less than the X-ray bunch separation time, so that no negative indices are required. The required total conversion gains of each camera can be obtained from ambient data. The terms beyond the first sum are due to the fact that the previously collected frames also contain after-images from prior frames. For example, subtracting only the previous frame from the frame of interest,

$$\mathcal{I}_{\text{real}}^N \simeq \frac{\mathcal{I}_{\text{coll}}^N}{\eta(t', \delta t)\chi^N} - F_1 \frac{\mathcal{I}_{\text{coll}}^{N-1}}{\eta(t', \delta t)\chi^{N-1}}, \quad (6)$$

will actually also subtract a portion of $\mathcal{I}_{\text{real}}^{N-2}$, since $\mathcal{I}_{\text{coll}}^{N-1}$ contains an after-image of it. A term compensating for this oversubtraction is required, where the $\mathcal{I}_{\text{coll}}^{N-2}$ image is added back in with a pre-factor of F_1^2. This correction then ignores the fact that $\mathcal{I}_{\text{coll}}^{N-2}$ also contained after-images of prior bunches, and this series of corrections explains the proliferation of terms in equation (5), with each additional term alternating sign.

Since F_i decreases quickly with i, only terms with low indices will be important. For the 24-bunch mode with $\delta t = 140$ ns and $t' = 6$ ns, we could keep all terms that amount to a correction greater than 1% of the previous frames' signal by keeping only the following terms,

$$\mathcal{I}_{\text{real}}^N = \frac{\mathcal{I}_{\text{coll}}^N}{\eta(t', \delta t)\chi^N} - F_1 \frac{\mathcal{I}_{\text{coll}}^{N-1}}{\eta(t', \delta t)\chi^{N-1}}$$
$$- \left(F_2 - F_1^2\right) \frac{\mathcal{I}_{\text{coll}}^{N-2}}{\eta(t', \delta t)\chi^{N-2}}. \quad (7)$$

In fact, the pre-factor of the third term, $(F_2 - F_1^2)$, nearly cancels (it is -0.012 for $\delta t = 140$ ns and $t' = 6$ ns), since subtracting $\mathcal{I}_{\text{coll}}^{N-1}$ in the first correction term actually subtracts slightly more of $\mathcal{I}_{\text{coll}}^{N-2}$ than is required for after-image correction. So, in this case, subtracting only the previous frame using the second term of equation (7) already corrects for the after-image from $\mathcal{I}_{\text{real}}^{N-2}$ to within 1.2% of the signal in $\mathcal{I}_{\text{real}}^{N-2}$, which may be sufficient. However, it may be advantageous to keep more terms, if any of the preceding images contain very bright features, such as bright, single-crystal diffraction peaks.

Applying equation (7) with only four frames of data, instead of N frames, presents a difficulty for the first and second frames collected, since the correction requires information from images collected prior to these. This can be worked around if the images prior to the first collected frame can be predicted. Specifically, if the sample were under ambient conditions during all X-ray exposures prior to the first frame, then ambient images taken prior to the experiment could be substituted for preceding dynamic images. This could be true if, for example, the first frame is precisely timed to initiation of the dynamic event (e.g. impact or detonation) and no modifications of the ambient pattern would be observed leading up to the event, say by a projectile traversing the beam. However, if no substitute is able to be applied for the missing preceding frames and only the available frames are included in the subtraction, then the second frame will be slightly over-corrected for the exposure prior to the first frame by 1.2% of that unrecorded image's intensity, and the first frame will have contamination of 17.8% of the preceding pulse and 2% of the image from two pulses prior.

In order to perform this subtraction, the images, $\mathcal{I}_{\text{coll}}^N$, from each of the cameras must first be spatially aligned, as described in Section 5, and the dark counts must be subtracted from each frame.

5. Alignment and distortion correction

Due to the different optical paths to each camera, the images must be corrected for alignment errors, as well as spatial distortion from the taper and optics. In particular, the mapping of pixel locations to locations on the X-ray phosphor will differ for each camera, potentially showing differences in magnification, translation, rotation, and in distortion. To accomplish this correction, the pixel locations of points in a known pattern are registered for each camera, four 20-parameter polynomial transformations are generated, and each image is transformed to remove spatial distortion and align each camera's field of view. The process outlined here is similar to that described by Barna *et al.* (1999), except the distortion transformation here is measured with visible light and a global transformation is determined rather than a local polynomial transformation. This process is repeated every time the system is modified, *e.g.* by changing the phosphor plate or fiber taper.

The mapping of pixel locations on the CCD to positions on the X-ray phosphor requires a known pattern to be placed in the plane of the X-ray phosphor. This process is performed with visible light, rather than X-ray illumination, so that this image registration may be performed during times when the X-ray beam is off. To this end, the X-ray phosphor-coated plate is removed, and a large patterned glass plate is attached in its place. The plate is covered by a regular grid of dots, 1 mm in diameter, separated by 1 mm (grid: Edmund Optics 59-217) for the smaller fiber taper and separated by 2 mm (grid: Edmund Optics 58-507) for the 120 mm and 150 mm fiber tapers. Because the visible input light is not present in the lens imaging section, having been absorbed at the image intensifier, differences in chromatic aberration between the input light and X-ray phosphor emission will not be present. Fig. 5(*a*) shows an example of an image collected in this way using the large fiber taper. The right side of this panel shows an exploded view of a small section of this image to highlight the image distortion — while the real dot pattern has a linear arrangement of dots, the image shows lines of dots that are clearly curved. Fig. 5(*b*) shows one quadrant of a difference image between the pattern collected from the first camera and the second, demonstrating that the two optical paths have different magnification and alignment before the images are corrected. The optical paths can be corrected to have the same magnifications, but this example demonstrates that the procedure is robust to a range of magnifications.

After collecting the images of the dot-grid, the pixel locations of the dot centers are located for each camera. This is done by fitting a two-dimensional Gaussian to each dot, producing an array of dot center pixel locations, $\mathbf{P}_{ij} = (x_{ij}, y_{ij})$, for each camera index, i, and each dot index, j. The desired pixel locations, $\mathbf{Q}_j = (x'_j, y'_j)$, of a regular, linear grid are then specified, the same for all cameras. This reference grid will determine the final scaling and orientation of all four camera images. A transformation, $\mathcal{T}_i(\mathbf{P}_{ij})$, is then determined for each camera to most closely transform each image's dot locations, $\mathbf{P}_{ij}$, to the desired dot locations of a reference grid, $\mathbf{Q}_j$,
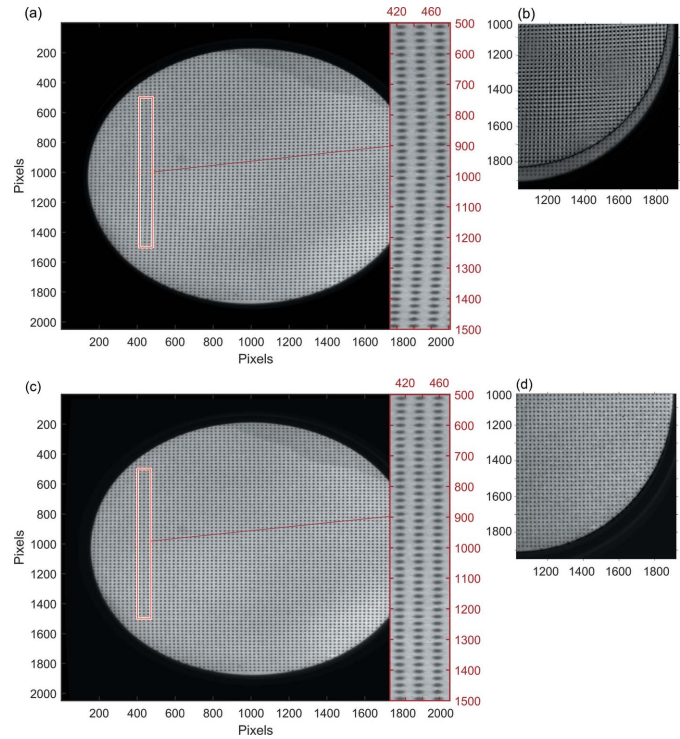

Figure 5
Example of a dot-grid calibration image and distortion correction. (*a*) The dot pattern image used for registration and distortion correction is shown before post-processing. The grid was placed on the 150:40 mm fiber taper. The dots are 1 mm in diameter, with 2 mm center separation. The area in the red box is shown in an exploded view on the right, demonstrating the spatial distortion, as the dots deviate from a linear arrangement. (*b*) A difference image from the first and second cameras compares the images before correction, displaying the difference in magnification, translation, and rotation. (*c*) The image from camera 1 is shown after post-processing, displaying the restoration of a linear arrangement of the dots after the spatial transformation. (*d*) The difference image between camera 1 and camera 2 is shown after post-processing, showing no difference in alignment or scaling.

mapping the four distorted grids to the reference grid. A third-order polynomial is used for $\mathcal{T}_i(\mathbf{P}_{ij})$, with a total of twenty coefficients a_k^i and b_k^i for each camera, such that

$$
\begin{aligned}
x'_j = {} & a_1^i x_{ij}^3 + a_2^i x_{ij}^2 y_{ij} + a_3^i x_{ij} y_{ij}^2 + a_4^i y_{ij}^3 + a_5^i x_{ij}^2 + a_6^i x_{ij} y_{ij} \\
& + a_7^i y_{ij}^2 + a_8^i x_{ij} + a_9^i y_{ij} + a_{10}^i, \\
y'_j = {} & b_1^i x_{ij}^3 + b_2^i x_{ij}^2 y_{ij} + b_3^i x_{ij} y_{ij}^2 + b_4^i y_{ij}^3 + b_5^i x_{ij}^2 + b_6^i x_{ij} y_{ij} \\
& + b_7^i y_{ij}^2 + b_8^i x_{ij} + b_9^i y_{ij} + b_{10}^i.
\end{aligned}
\tag{8}
$$

This general transformation was chosen, over one specific to a type of distortion (*e.g.* barrel distortion from a lens), to allow multiple sources of distortion to be corrected at once, taking into account the potentially irregular distortion of the fiber taper as well as any lens distortions. This transformation is determined in *MATLAB* (Mathworks Inc.) using the *fitgeotrans* function, and the transformation is applied to each image using the *imwarp* function, using linear interpolation to resample the intensity values. Fig. 5(*c*) shows the same image from Fig. 5(*a*), after this transformation is applied, where the

exploded view demonstrates the realignment of the dots to a linear grid. By aligning the dot locations from each camera to the same grid, the transformations simultaneously accomplish the task of re-scaling, translating, and rotating the images. Fig. 5(d) shows the same comparison as Fig. 5(b) after data correction, demonstrating that the correction has given the second camera the same scaling and alignment as the first camera. To quantify the remaining distortion, we compare the transformed dot center positions with that of a regular grid. The dot-finding algorithm was run on the corrected images to determine pixel locations for the transformed dot centers. The desired dot-center pixels were then generated from a regularly spaced grid with a common center dot location as the data, and the distance between the desired and transformed dot locations were calculated. The mean distance between the dot center locations and the regular grid locations was 0.6 pixels, with a standard deviation of 0.4 pixels.

The orientation and scaling of the reference grid must be specified. The orientation is chosen to align the pixel columns to a known vertical axis in the experiment. Most often, this is done by taking an X-ray image of a metal plumb line. Then, the rotation of the reference grid, $\mathbf{Q}_j$, may be specified so that the transformation orients the plumb line feature to be vertical in the output images. The scaling of the reference grid determines the final conversion from pixel spacing to distance on the phosphor. This scaling is chosen to closely match that of the original uncorrected image, to minimize the change in image size. The conversion is specified to be 23 pixels mm^{-1} on the phosphor for the 75:40 mm fiber taper, 14.5 pixels mm^{-1} for the 120:40 mm fiber taper, and 11.5 pixels mm^{-1} for the 150:40 mm fiber taper. This re-scaling also allows a uniform magnification for users between experimental campaigns, countering the possibility that the real magnifications may change slightly as this system is adjusted to accommodate modifications over time.

6. Detector DQE

To compare the performance of this detector system with other detectors, we can quantify the response of this detector to X-ray photons and the signal-to-noise ratio (SNR) with varying levels of illumination. First, we must note that the response of this detector system varies dramatically between configurations: as the X-ray phosphor plate is changed, the fiber taper demagnification is changed, or as the image intensifier gain is changed. However, as a guide for the achievable sensitivity, the most sensitive configuration was calibrated to relate detector counts to incident X-ray photons, and the variance of repeated measurements is used to measure the DQE, comparing its performance against an ideal detector. Unfortunately, beam intensity fluctuations during these measurements contaminate this measurement and prevent precise measurement of the DQE, but the measurements can still be used to constrain the DQE with careful consideration of the effect of beam fluctuations. With approximate parameters of each stage of the conversion

process, the DQE of this configuration is also predicted to provide context for this measurement.

For calibration, the four-frame detector was configured with the 75:40 mm fiber taper, the external image intensifier at maximum gain (specified at 4000 W_{out}/W_{in}), and one of our most sensitive X-ray phosphor plates (having an areal density of 81 mg cm^{-2}). With this configuration, a single 23 keV X-ray photon striking the detector produced 4300 counts on one of the ICCD cameras. With this calibration, the DQE can be measured as the the ratio of the squared, measured SNR, to the squared, ideal SNR, assuming Poisson statistics of the incoming photons. For example, for 50 repeated images of this masked region, the total counts in the region of interest are measured. With a mean of 3300 X-ray photons in the unmasked region and a standard deviation of 106 X-ray photons, this would suggest a DQE of 0.29. However, there is a significant contribution to this variation from temporal variation of the incident beam intensity. After careful consideration of the contribution of these fluctuations to the measurement (presented in the supporting information), we conclude that a reasonable estimate for the detector DQE with this configuration is between 40% and 60%. For comparison, a noiseless detector would have a DQE equal to the QE, which in this case is estimated to be 0.92, using the 81 mg cm^{-2} areal density of this phosphor coating (Berger et al., 2010).

As a point of comparison, estimated parameters from each detector component can be used to predict a DQE for this system. Using an approach similar to that presented by Vartsky et al. (2009), published parameters for LSO:Ce (Syntfeld-Kazuch et al., 2009; Wanarak et al., 2012), and estimated or manufacturer-specified parameters for the ICCDs and front-end image intensifier, yields a prediction of about 20% to 30% for the DQE. The lower estimate corresponds to the expected lower range of each image intensifier's noise performance. Details of this calculation are presented in the supporting information. However, the two most influential parameters in that calculation are very uncertain, specifically the noise factor of the first image intensifier and the losses in the phosphor and fiber coupling to that intensifier. The losses are determined indirectly by presumed knowledge of the conversion gain of each of the other conversion stages, and increased losses before the first image intensifier will magnify the effect of its noise. If, for example, there were lower gains downstream of the intensifier photocathode amounting to a factor of two (e.g. due to lower than specified gain, increased losses in the lenses, etc.), it would raise the estimate from 30% to 45%.

While this DQE estimate does not necessarily enhance our degree of certainty of the DQE measurements, it does highlight potential areas of improvement. In particular, the first image intensifier has a large effect on the total noise, and the dominant cause is the 13% QE of the S20 photocathode on that device. A photocathode that is better matched to the spectral output of the X-ray phosphor could dramatically improve the DQE of the entire detector system. Furthermore, since the contribution of this image intensifier to the total

DQE can be reduced by more quanta arriving at its photo-cathode, reducing the losses leading up to this intensifier would improve the DQE considerably.

Despite the apparent discrepancy between measurement and prediction, we can use this model to examine the expected DQE change from different configurations of the system, remembering that the real result may be slightly higher than predicted. Specifically, if we change the fiber optic taper, allowing for a 120 mm or 150 mm diameter field of view, this is associated with much greater losses prior to the image intensifier giving a decrease in total signal level of a factor of 2.7 and 8, respectively (the large discrepancy is due to a much longer taper for 150 mm, coupled with the glass absorption). Beginning with the parameters that yielded a 30% DQE estimate, the DQEs resulting from increasing the losses prior to the intensifier by these factors are 14% for the 120:40 mm taper and 5% for the 150:40 mm taper. Accordingly, the 150 mm taper is only recommended for experiments that absolutely require a larger field of view.

7. Spatial resolution and dynamic range

With the calibration of the total conversion gain from Section 6, *i.e.* 4300 counts per incident X-ray photon for the 75 mm active area configuration, the dynamic range can be found by simply dividing the maximum counts per pixel in the ICCD before saturating the analog-to-digital conversion (ADC), 2^{16}, by this gain, yielding 15 X-ray photons per pixel for this configuration [where each pixel represents $(43 \, \mu m)^2$ on the phosphor]. Similarly, using the 120 mm and 150 mm active area configurations, with the increased losses in the fiber taper, the dynamic range is 40 X-ray photons per pixel and 120 X-ray photons per pixel. This would be the photon fluence required to saturate the ADC if the detector were uniformly illuminated. However, the spatial resolution must be discussed to consider the maximum brightness of localized features, since localized features would have their signal spread over many pixels.

While the resolution can vary as the detector is reconfigured and optimized, when configured for a 75 mm active area, the FWHM of the point-spread function is typically 220 μm (5 pixels). The spatial resolution is limited by the optical path subsequent to the fiber optics, *i.e.* the image intensifier and the imaging optics. Accordingly, for differing fiber optic taper size, the spatial resolution scales with the active area diameter, while remaining the same size in camera pixels. For the purpose of estimating the spreading of a localized signal over many pixels for a dynamic range calculation, the shape can be estimated as a 2D circular Gaussian ($\sigma = 2.1$ pixels) so that the signal in the central pixel is only 3.6% of the total signal. Accordingly, a spatially localized signal (*e.g.* a very sharp diffraction peak) could contain as many as 420 photons without saturating the ADC with the 75 mm active area configuration. Considering the additional losses in the larger fiber tapers, the 120 mm and 150 mm active area configurations would saturate with a localized flux of 1100 and 3300 incident photons, respectively.

8. Representative data

Diffraction data from two different impact experiments will be shown to demonstrate aspects of the system. The first shows the sensitivity of the detector in the context of a typical target with small, disordered grains, which will generally have more diffuse, lower-intensity peaks. The second example demonstrates the application of the after-image subtraction method described in Section 4.

Figs. 6(*a*)–6(*c*) show images of the XRD pattern from a copper sample, sapphire interferometry window, and a LiF(100) impactor. The copper diffraction rings are generated by the 23 keV beam passing through 152 μm of copper, which is then attenuated by 2.494 mm of sapphire and 5.77 mm of LiF, which are necessary for the shock experiment. The first image shows the XRD pattern from the sample prior to the shot, under ambient conditions. The following two frames show the sample 13 ns and 167 ns after the LiF impacts the Cu sample at 1481 m s^{-1}. Two additional images were collected during this experiment, but they are not displayed due to their visual similarity to the previous frames. These images were collected with the 75:40 mm fiber taper. This thickness of copper is much thicker than optimal for generating a strong XRD pattern, as it only transmits about 5% of the incident beam. However, the pattern remains bright enough to extract crystal *d*-spacings and to discern crystal texture information from the intensity modulation around the rings. Fig. 6(*d*) shows the integrated (111) and (200) peaks under ambient conditions and in each of the frames after impact. The diffraction peaks for the shocked copper are shifted to higher 2θ in the first two frames after impact, consistent with compression. In the following two frames, the peaks shift to lower angle as the release wave from the back of the sapphire reaches the Cu. Since detailed analysis of an impact experiment is complex and beyond this article's scope, for examples of analyses of similar XRD patterns, we refer the interested reader to articles analyzing similar patterns from this detector (Williams *et al.*, 2020; Renganathan *et al.*, 2019; Newman *et al.*, 2018; Turneaure *et al.*, 2018; Tracy *et al.*, 2018). This example provides a good demonstration of the utility of multiframe collection, even in short-duration experiments. While only one of these frames would suffice to, for example, determine the *d*-spacing at the peak pressure, it would be very fortunate to collect a single image at precisely the right time, but with four frames there is a higher chance of collecting the ideal frame. In this case, the frame at 167 ns after impact provides a measurement of the crystal structure after the ring-up to the peak pressure of 18.8 GPa, and this was the objective of the experiment. However, the other three frames provide the necessary context to verify this, showing that the release wave does not reach the Cu until later frames.

Currently, the typical beam configuration for diffraction at the DCS has a peak energy of 23.5 keV with a FWHM of 0.8 keV, with an asymmetric shape that can be seen in the asymmetric profiles of Fig. 6(*d*). The beam is filtered by Kirkpatrick–Baez mirrors to only pass a single harmonic. This configuration is typically sufficient to resolve peaks of shocked
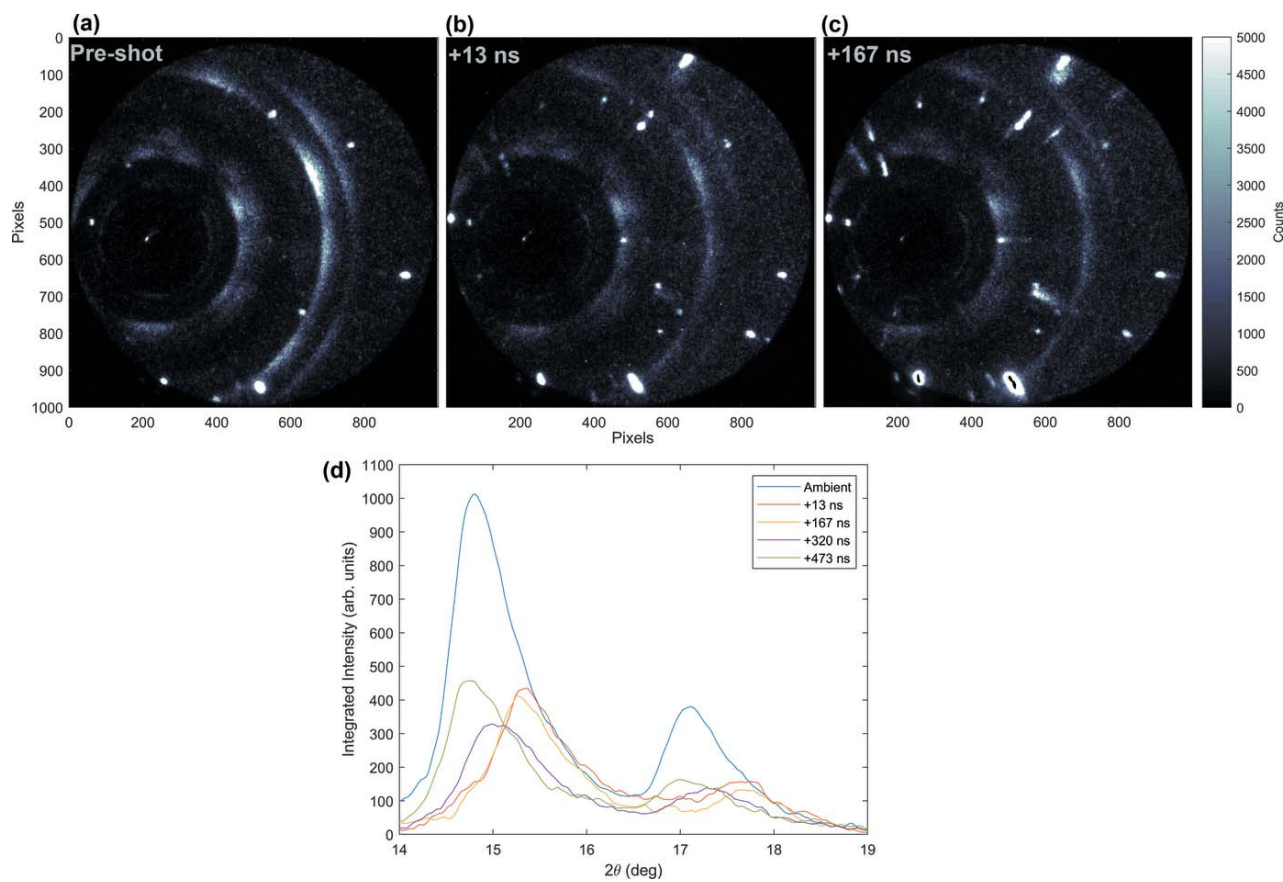
Figure 6
Example Dynamic X-ray diffraction patterns from copper during a plate-impact experiment at the DCS. (*a–c*) Images from the DCS four-frame XRD detector capture XRD patterns from a copper sample, an a-cut sapphire interferometry window, and a LiF impactor, as the Cu is compressed to 18.8 GPa. The 23 keV beam passes through 152 μm of Cu, 2.494 mm of sapphire, and 5.77 mm of LiF to produce this pattern. Each image is produced from a single 90 ps-duration X-ray exposure. (*a*) The first image was taken before the shot, showing the XRD pattern under ambient conditions, and the subsequent two images show the evolved pattern (*b*) 13 ns after impact and (*c*) 167 ns after impact. The brightness scaling of the figure is chosen to emphasize the weaker powder rings from the copper, while the single-crystal peaks from the LiF and sapphire are well above this scale. The plot in (*d*) shows the integrated intensity versus 2*θ* for the (111) and (200) Cu reflections, under ambient conditions and in each frame after impact. The shocked reflections are shifted to higher 2*θ* in the first two frames after impact, consistent with compression, and in the following frames the peaks shift to lower angle as the release wave from the back of the sapphire reaches the Cu.

and ambient crystals, and for applications requiring better resolution an undulator configuration is also available with narrower bandwidth (0.4 keV FWHM at 23 keV) with slightly reduced flux. In XRD studies to date, the system has exclusively been used to examine peak positions and shapes resulting from materials with crystalline order or to demonstrate the lack of this order. While studies examining the radial electron distribution in amorphous materials or liquids are possible with this detector, the analysis would be complicated by the broad, asymmetric shape of the undulator harmonic as well as the likely overlap of the diffuse ambient and shocked scattering.

A second set of data with bright single crystal peaks illustrates the degree to which the after-images, described in Section 3, may be subtracted with the method described in Section 4. Fig. 7 shows dynamic XRD data during the shock-compression of highly oriented pyrolytic graphite (HOPG). These data have been previously presented by Turneaure *et al.* (2017), which demonstrated the transformation of graphite to hexagonal diamond, and the present analysis will focus only

on the efficacy of the after-image subtraction method, which was not applied in that work. Figs. 7(*a*)–7(*b*) show two raw dynamic XRD frames, as the HOPG is being compressed, without an after-image correction. The pattern in Fig. 7(*a*) was collected 144 ns after impact when the shockwave has passed through 47% of the sample. The localized, bright peaks are from ambient HOPG, while the shocked state has dimmer, diffuse peaks. Fig. 7(*b*) was collected just as the shockwave is reaching the back of the HOPG, so that 98% of the HOPG has been shocked. The bright ambient peaks remaining in Fig. 7(*b*) are far too bright to come from 2% of the HOPG thickness – these are the after-images of the peaks from the previous exposure. The inset shows an exploded view of two of these peaks, on either side of one of the diffuse peaks from the shocked state. In order to remove these peaks, Turneaure *et al.* (2017) simply subtracted an empirical fraction of the ambient pattern. Using the recipe in Section 4, the same results can be achieved without this free parameter.

The distortion correction is first applied, aligning the images of each camera. The pattern shown in Fig. 7(*b*) is actually the
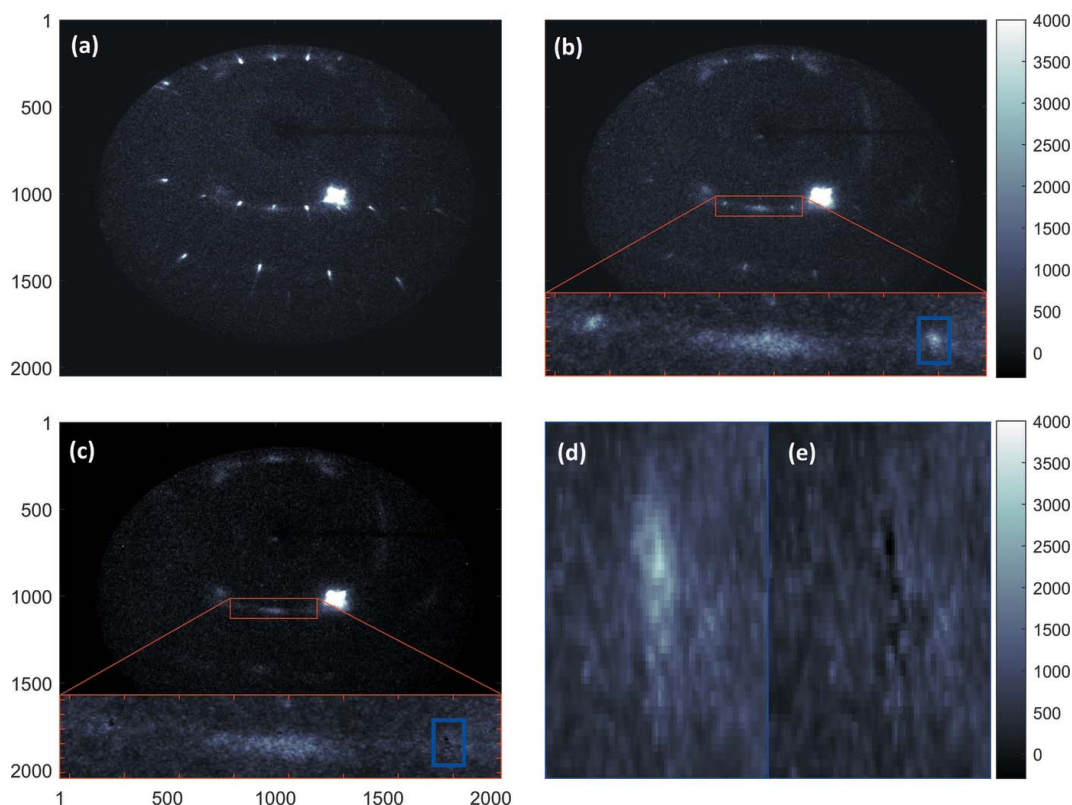
Figure 7
Dynamic X-ray diffraction data showing after-image subtraction. (*a*–*b*) Two frames of XRD data collected during shock compression of HOPG are shown, with no after-image subtraction. (*a*) The XRD pattern from the sample is shown, 144 ns after impact with 47% of the HOPG compressed. The bright peaks throughout the image are from the remaining ambient HOPG. (*b*) The XRD pattern from the subsequent frame, at 297 ns after impact with 98% of the HOPG compressed. The bright peaks should be essentially gone, yet they remain visible due to the after-image of the previous exposure. The inset shows an exploded view with two of these peaks. The diffuse peak in the center of the inset is from the shocked state. (*c*) The image from (*b*) is shown after the after-image subtraction is applied, showing that the peaks are removed. (*d*–*e*) Exploded views of the peak in the blue box from (*b*–*c*), before and after subtraction, displaying a slight oversubtraction in some pixels and under-subtraction in others. This data was explored in detail by Turneaure *et al.* (2017), where these peaks were removed by subtracting an empirical fraction of the ambient image.

third in the sequence, so that equation (7) may be applied using the first and second frames in the sequence. Fig. 7(*c*) shows the image resulting from the subtraction, clearly lacking the ambient peaks. Figs. 7(*d*)–7(*e*) show an exploded view of the single peak within the blue box in Figs. 7(*b*)–7(*c*), before and after subtraction. It is clear from Fig. 7(*e*) that some pixels have been over-subtracted significantly, while others seem to retain some intensity from the after-image. This is due to the slightly different shapes of the peak on each of the cameras, either due to slight differences in focusing or the significant amount of noise in the images. So, this is not a perfect approach, and it is most appropriate when it is the integrated intensity of the peak that is of interest, rather than the per-pixel intensity values. The total counts in the peak shown in Fig. 7(*d*) is 358 kcounts s^{-1} above the neighboring areas, and after the subtraction it is 10 kcounts s^{-1} under the surrounding areas. An example of the application of this subtraction technique is presented by Mandal *et al.* (2020), where the authors follow this recipe for after-image subtraction to quantify the evolution of the total diffracted intensity in the entire (111) Debye–Scherrer ring to determine the fraction of melted material.

9. Conclusion

The four-frame diffraction detector system at the Dynamic Compression Sector provides a time-resolved, indirect X-ray detection system, designed to capture four frames of X-ray diffraction data from a single experiment with a temporal resolution of 90 ps, the X-ray exposure duration. The multi-frame capability is achieved by splitting the image from an X-ray phosphor to four time-resolved ICCD cameras. This multi-frame ability allows a margin of error for impact timing with respect to the detector triggering as well as providing a more complete view of the dynamics. With additional gain provided by an image intensifier to compensate for the optical losses, the detector has sufficient sensitivity to acquire powder diffraction patterns from single X-ray bunches in the '24-bunch' mode of the APS storage ring.

While splitting the image to multiple cameras enables the multiframe capability, it also introduces a few complications. The additional image intensifier introduces a second phosphor decay in series with the X-ray phosphor decay. Due to these sequential decays, the detector shows a significant amount of after-image contamination from the previous X-ray pulses,

which depends on the precise ICCD gate timing parameters used during the experiment. A procedure has been provided to determine the optimal gate timing and to subtract after-images to correct the collected data. This subtraction procedure is most useful when the integrated intensity of a feature (*e.g.* a total XRD peak intensity) is of interest, rather than the precise 2D shape of a small feature, as the per-pixel noise can be too large for a high-fidelity after-image subtraction. Additionally, the lenses and fiber taper both contribute to a spatial distortion in mapping positions on the X-ray phosphor to pixels on the ICCD. However, using a reference grid, the distortion is corrected and the images are transformed to have the same translation, rotation, and scaling.

The noise level of the detector has been roughly quantified with variance measurements and determined to be consistent with a DQE of approximately 0.4 to 0.6 for the 75 mm active-area configuration (the most sensitive configuration). While this measurement is coarse due to fluctuations in the input beam intensity, this number is comparable with the maximum DQE that could be obtained with a silicon direct detector with 0.5 mm silicon at this X-ray photon energy (QE = 0.28 for 23.5 keV X-rays) (Berger *et al.*, 2010). Estimates of the expected DQE from the characteristics of each detector stage suggest that significant performance improvements would be achieved by improvement to the QE of the front-end image intensifier photocathode or reduced losses in the fiber optic taper leading to this photocathode.

10. Related literature

The following references, not cited in the main body of the paper, have been cited in the supporting information: Bell (1975); Longobardi *et al.* (1994); Gruner *et al.* (2002).

References

Allahgholi, A., Becker, J., Delfs, A., Dinapoli, R., Goettlicher, P., Greiffenberg, D., Henrich, B., Hirsemann, H., Kuhn, M., Klanner, R., Klyuev, A., Krueger, H., Lange, S., Laurus, T., Marras, A., Mezza, D., Mozzanica, A., Niemann, M., Poehlsen, J., Schwandt, J., Sheviakov, I., Shi, X., Smoljanin, S., Steffen, L., Sztuk-Dambietz, J., Trunk, U., Xia, Q., Zeribi, M., Zhang, J., Zimmer, M., Schmitt, B. & Graafsma, H. (2019). *J. Synchrotron Rad.* **26**, 74–82.

Bagge-Hansen, M., Lauderbach, L., Hodgin, R., Bastea, S., Fried, L., Jones, A., van Buuren, T., Hansen, D., Benterou, J., May, C., Graber, T., Jensen, B. J., Ilavsky, J. & Willey, T. M. (2015). *J. Appl. Phys.* **117**, 245902.

Barna, S. L., Tate, M. W., Gruner, S. M. & Eikenberry, E. F. (1999). *Rev. Sci. Instrum.* **70**, 2927–2934.

Becker, J., Tate, M. W., Shanks, K. S., Philipp, H. T., Weiss, J. T., Purohit, P., Chamberlain, D. & Gruner, S. M. (2016). *AIP Conf. Proc.* **1741**, 040037.

Bell, R. L. (1975). *IEEE Trans. Electron Devices*, **22**, 821–829.

Berger, M., Hubbell, J., Seltzer, S., Chang, J., Coursey, J., Sukumar, R., Zucker, D. & Olsen, K. (2010). *XCOM: Photon Cross Section Database* (Version 1.5), http://physics.nist.gov/xcom.

Ciamberlini, C., Longobardi, G., Ramazza, P. L. & Residori, S. (1994). *Opt. Eng.* **33**, 845.

Gruner, S. M., Tate, M. W. & Eikenberry, E. F. (2002). *Rev. Sci. Instrum.* **73**, 2815–2842.

Gupta, Y. M., Turneaure, S. J., Perkins, K., Zimmerman, K., Arganbright, N., Shen, G. & Chow, P. (2012). *Rev. Sci. Instrum.* **83**, 123905.

Hart, M., Angelsen, C., Burge, S., Coughlan, J., Halsall, R., Koch, A., Kuster, M., Nicholls, T., Prydderch, M., Seller, P., Thomas, S., Blue, A., Joy, A., O'Shea, V. & Wing, M. (2012). *2012 IEEE Nucl. Sci. Symp. Med. Imaging Conf. Rec. (NSS/MIC)*, pp. 534–537. IEEE.

Lambert, P. K., Hustedt, C. J., Casem, D. T., Sinclair, N., Zhang, X. J., Lee, K. M., Leong, A. F., Schuster, B. E. & Hufnagel, T. C. (2020). *Metall. Mater. Trans. A*, **51**, 5101–5109.

Luo, S. N., Jensen, B. J., Hooks, D. E., Fezzaa, K., Ramos, K. J., Yeager, J. D., Kwiatkowski, K. & Shimada, T. (2012). *Rev. Sci. Instrum.* **83**, 073903.

Mandal, A., Jensen, B. J., Hudspeth, M. C., Root, S., Crum, R. S. & Akin, M. C. (2020). *Phys. Rev. Mater.* **4**, 063604.

Newman, M. G., Kraus, R. G., Akin, M. C., Bernier, J. V., Dillman, A. M., Homel, M. A., Lee, S., Lind, J., Mosenfelder, J. L., Pagan, D. C., Sinclair, N. W. & Asimow, P. D. (2018). *Geophys. Res. Lett.* **45**, 8129–8135.

Philipp, H. T., Tate, M. W., Purohit, P., Chamberlain, D., Shanks, K. S., Weiss, J. T. & Gruner, S. M. (2016). *AIP Conf. Proc.* **1741**, 040036.

Rayonix LLC, (2021). *SX165 – Rayonix, LLC*, https://www.rayonix.com/product/sx-165/.

Renganathan, P., Turneaure, S. J., Sharma, S. M. & Gupta, Y. M. (2019). *Phys. Rev. B*, **99**, 134101.

Sajaev, V. V. (2010). *APS Storage Ring Parameters*, http://www.aps.anl.gov/Accelerator_Systems_Division/Accelerator_Operations_Physics/SRparameters/node6.html.

Syntfeld-Kazuch, A., Moszyński, M., Świderski, Ł., Szczesniak, T., Nassalski, A., Melcher, C. L., Spurrier, M. A., Goliszek, B., Kamiński, P. & Nowaczyk, M. (2009). *IEEE Trans. Nucl. Sci.* **56**, 2972–2978.

Tracy, S. J., Turneaure, S. J. & Duffy, T. S. (2018). *Phys. Rev. Lett.* **120**, 135702.

Turneaure, S. J., Sharma, S. M. & Gupta, Y. M. (2018). *Phys. Rev. Lett.* **121**, 135701.

Turneaure, S. J., Sharma, S. M., Volz, T. J., Winey, J. M. & Gupta, Y. M. (2017). *Sci. Adv.* **3**, eaao3561.

Turneaure, S. J., Sinclair, N. & Gupta, Y. M. (2016). *Phys. Rev. Lett.* **117**, 045502.

Vartsky, D., Feldman, G., Mor, I., Goldberg, B., Bar, D. & Dangendorf, V. (2009). *J. Instrum.* **4**, P02001.

Wanarak, C., Chewpraditkul, W. & Phunpueok, A. (2012). *Proc. Eng.* **32**, 765–771.

Williams, C. L., Kale, C., Turnage, S. A., Shannahan, L. S., Li, B., Solanki, K. N., Becker, R., Hufnagel, T. C. & Ramesh, K. T. (2020). *Phys. Rev. Mater.* **4**, 083603.